Model-Based Range Extension Control System for Electric Vehicles With Front and Rear Driving–Braking Force Distributions

Hiroshi Fujimoto, *Senior Member, IEEE*, and Shingo Harada, *Student Member, IEEE*

***Abstract*—This paper proposes a model-based range extension control system for electric vehicles. The proposed system optimizes the front and rear driving–braking force distributions by considering the slip ratio of the wheels and the motor loss. The optimal distribution depends solely on vehicle acceleration and velocity. Therefore, this system is effective not only at constant speeds but also in acceleration and deceleration modes. Bench tests were conducted for more precise evaluation and to realize experimental results with high reproducibility. The effectiveness of the proposed system was verified through field and bench tests.**

***Index Terms*—Bench test, driving and braking force distribution, electric vehicle (EV), range extension control system (RECS).**

I. Introduction

BASED on current environmental and energy problems, electric vehicles (EVs) have been proposed as an alternative solution to internal combustion engine vehicles (ICEVs). EVs have remarkable advantages in motion control compared with ICEVs [1] as follows.

- The response to the driving–braking force by the motor is much faster than that of engines (about 100 times).
- In-wheel motors enable independent control and drive of each wheel.
- The motor torque is precisely measured from the motor current.

Research is actively ongoing on traction control [2], [3] and stability control [4], [5] to utilize the above advantages.

One reason that is preventing EVs from spreading is that its mileage per charge is shorter than that of conventional ICEVs. In order to solve this problem, wireless power transfer for moving vehicles [6], [7] is being researched. As another approach, ultracapacitors are being utilized for energy storage systems to improve the energy regeneration [8]–[10]. Research is also being carried out to improve the efficiency of motors [11]. In order to realize high-efficiency motor control, Inoue *et al.* examined torque and angular velocity patterns that maximize efficiency during acceleration and deceleration [12]. Yuan and Wang utilized the independent characteristics of traction motors to develop a torque distribution method for decreasing EV energy consumption where two motors with the same efficiency characteristics are used [13].

The authors' research group previously proposed the range extension control system (RECS) [14]–[16], which does not involve changes to the vehicle structure such as an additional clutch [13] or the motor type. Instead, the RECS extends the cruising range of a vehicle by motion control. We assumed that an EV has more than one motor and that suitable torque distribution results in improved efficiency.

Two types of RECS have already been proposed. The first involves optimizing the driving force distribution ratio between front and rear motors when the vehicle runs on a straight road [15], [16]. The second involves optimizing the distribution ratio between left and right motors when the vehicle is curving [14].

This paper assumed that the straight road and the steering angle is fixed to zero. Although the work in [15] assumes that the vehicle speed is constant, Harada and Fujimoto in [16] evaluated in terms of the acceleration and deceleration on a straight road. The effectiveness of the proposed system was only verified for operation at low speeds. It has not been verified for operation at high speeds, where the ratios of the driving resistance and motor iron loss to the total loss are relatively large. Therefore, experiments on operation at high speeds are necessary for a more appropriate evaluation of the RECS. In this paper, a bench test was performed to realize high reproducibility of the results along with a field test to evaluate the proposed system. The effectiveness of the proposed system was verified through the field and bench tests.

II. Experimental Vehicle and Vehicle Model

A. Experimental Vehicle

This study used the original EV "FPEV-2 Kanon," which was developed in-house. This vehicle has four outer rotor-type in-wheel motors. Since these are direct-drive-type motors, the reaction force from the road is directly transferred to the motor without backlash from the reduction gear.

Manuscript received March 25, 2014; revised March 30, 2014 and August 24, 2014; accepted October 25, 2014. Date of publication February 11, 2015; date of current version April 8, 2015. This work was supported in part by the Industrial Technology Research Grant Program from the New Energy and Industrial Technology Development Organization (NEDO) of Japan under Grant 05A48701d and in part by the Ministry of Education, Culture, Sports, Science and Technology under Grant 22246057 and Grant 26249061.

The authors are with the Department of Advanced Energy, Graduate School of Frontier Sciences, The University of Tokyo, Chiba 277-8561, Japan (e-mail: hfuji@ieee.org).

Color versions of one or more of the figures in this paper are available online at http://ieeexplore.ieee.org.

Digital Object Identifier 10.1109/TIE.2015.2402634

TABLE I
VEHICLE SPECIFICATIONS

Vehicle mass M	854 kg
Wheelbase l	1.715 m
Distance from CG to front/rear axles l_f, l_r	l_f:1.013 m l_r:0.702 m
Gravity height h_g	0.51 m
Front wheel inertia J_{ω_f}	1.24 Nms^2
Rear wheel inertia J_{ω_r}	1.26 Nms^2
Wheel radius r	0.302 m

TABLE II
SPECIFICATIONS OF IN-WHEEL MOTORS

	Front	Rear
Manufacturer	TOYO DENKI SEIZO K.K.	
Type	Direct drive system Outer rotor type	
Rated torque	110 Nm	137 Nm
Maximum torque	500 Nm	340 Nm
Rated power	6.0 kW	4.3 kW
Maximum power	20.0 kW	10.7 kW
Rated speed	521 rpm	300 rpm
Maximum speed	1113 rpm	1500 rpm

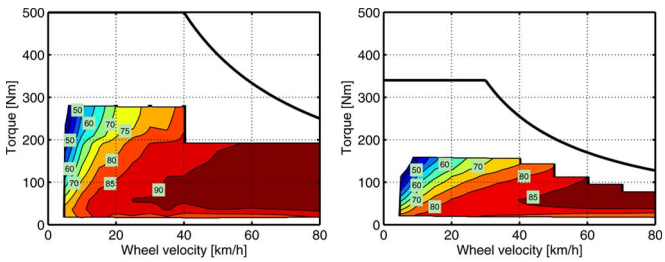

Fig. 1. Efficiency maps of front and rear motors. (a) Front motor. (b). Rear motor.

Tables I and II show the specifications of the vehicle and in-wheel motors. Fig. 1 presents the efficiency map of the front and rear in-wheel motors. In this paper, higher torque operation points where the motor torque was greater than one and a half times the rated torque were not used for the evaluation. Since the front and rear motors installed in the vehicle were different, their efficiency maps were also different. Therefore, the cruising range can be extended by employing the difference in efficiency.

Fig. 2 illustrates the power system of the vehicle. A lithium-ion battery was used as the power source. The voltage of the main battery was 160 V (ten battery modules were connected in series). The voltage was boosted to 320 V by a copper. In this paper, the copper loss was not evaluated because it was independent of the torque distribution.

B. Vehicle Model

The four-wheel-drive vehicle model is described here. The wheel rotation is expressed by (1). For straight driving, the driving–braking forces of the right and left wheels are equal.

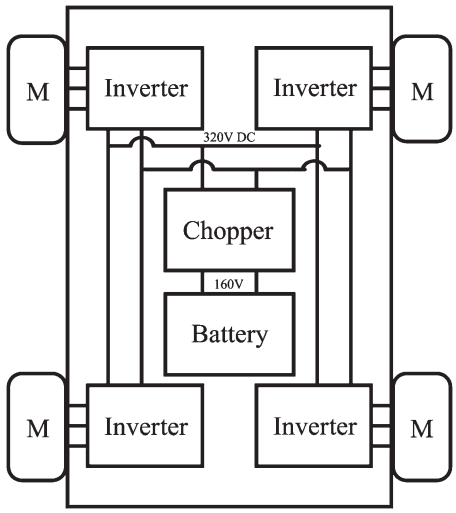

Fig. 2. Electric power system of a vehicle.

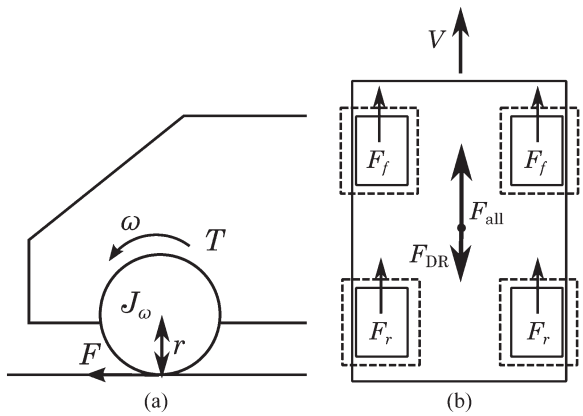

Fig. 3. Vehicle model. (a) Rotational motion of wheel. (b) Longitudinal motion of vehicle.

Therefore, the vehicle dynamics is expressed by (2) and (3). Thus,

$$J_{\omega_j}\dot{\omega}_j = T_j - rF_j \tag{1}$$

$$M\dot{V} = F_{\text{all}} - F_{\text{DR}} \tag{2}$$

$$F_{\text{all}} = 2\sum_{j=f,r} F_j \tag{3}$$

where ω_j is the wheel angular velocity, V is the vehicle speed, T_j is the motor torque, F_{all} is the total driving–braking force, F_j is the driving–braking force of each wheel, M is the vehicle mass, r is the wheel radius, J_{ω_j} is the wheel inertia, and F_{DR} is the driving resistance, as shown in Fig. 3. Subscript j represents f or r (f stands for front, and r represents rear).

Next, the slip ratio λ_j is defined as

$$\lambda_j = \frac{V_{\omega_j} - V}{\max\left(V_{\omega_j}, V, \epsilon\right)} \tag{4}$$

where $V_{\omega_j} = r\omega_j$ is the wheel speed, and ϵ is a small constant to avoid zero division. $\lambda_j > 0$ means driving, and $\lambda_j < 0$ means braking. The slip ratio λ is known to be related with the coefficient of friction μ, as shown in [17]. In region $|\lambda| \ll 1$, μ is nearly proportional to λ. By using the normal forces of

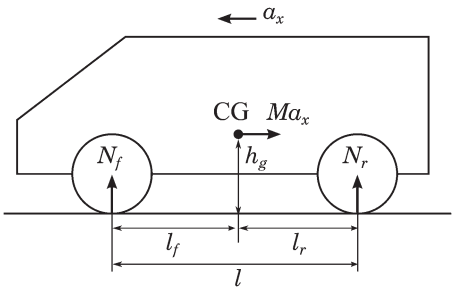

Fig. 4. Load transfer model.

each wheel N_j during longitudinal acceleration with a_x and the slope of the curve, the driving force of each tire is expressed as

$$F_j = \mu_j(\lambda_j)N_j(a_x) \approx D'_s\lambda_j N_j(a_x) \tag{5}$$

where D'_s is the normalized driving stiffness [20].

As shown in Fig. 4, the normal forces of each wheel during the longitudinal acceleration process are calculated as follows:

$$N_f(a_x) = \frac{1}{2}\left(\frac{l_r}{l}Mg - \frac{h_g}{l}Ma_x\right) \tag{6}$$

$$N_r(a_x) = \frac{1}{2}\left(\frac{l_f}{l}Mg + \frac{h_g}{l}Ma_x\right) \tag{7}$$

where N_f and N_r are the front and rear normal forces, respectively; l_f and l_r are the distances from the center of gravity to the front and rear axles, respectively; and h_g is the height of the center of gravity. The acceleration direction is defined as positive when the vehicle is accelerating.

C. Driving–Braking Force Distribution Model

During straight driving, the required total driving–braking force can be distributed to each wheel. Since the EV motors were assumed to be independently controlled in this study, the driving–braking force distribution has an extra degree of freedom. By introducing the front and rear driving–braking force distribution ratio k, the driving–braking forces can be formulated based on the total driving–braking force $F_{\rm all}$ and the distribution ratio k as follows [15]:

$$F_j(k) = \frac{1}{2}\gamma_j(k)F_{\rm all} \tag{8}$$

$$\gamma_j(k) = \begin{cases} 1-k, & j = f \\ k, & j = r. \end{cases} \tag{9}$$

The distribution ratio k varies from 0 to 1. $k = 0$ means that the vehicle is a front-driven system, and $k = 1$ means that it is only rear driven. Note that, even if the driving force F_j is zero, the torque T_j is not always zero according to (1).

D. Modeling of Inverter Input Power

The slip ratio and motor loss can be considered to derive the distribution ratio that minimizes the inverter input power. Neglecting the inverter loss and mechanical loss of the motor, the inverter input power $P_{\rm in}$ is expressed as

$$P_{\rm in} = P_{\rm out} + P_c + P_i \tag{10}$$

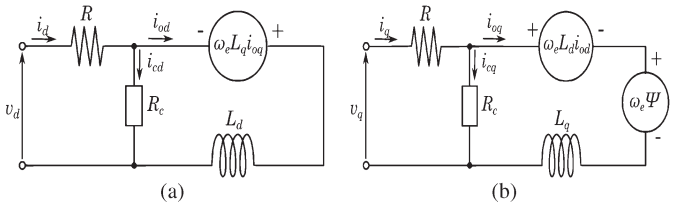

Fig. 5. Equivalent circuit of a permanent-magnet synchronous motor for the iron loss model. (a) d-axis. (b) q-axis.

where $P_{\rm out}$ is the sum of the mechanical output of each motor, P_c is the sum of the copper loss of each motor, and P_i is the sum of the iron loss of each motor. $P_{\rm out}$ is given by

$$P_{\rm out} = 2\sum_{j=f,r}\omega_j T_j. \tag{11}$$

The sum of the copper loss of the permanent-magnet motors P_c can be modeled as

$$P_c = 2\sum_{j=f,r} R_j\left(i_{qj}^2 + i_{dj}^2\right) \simeq 2\sum_{j=f,r} R_j i_{qj}^2 \tag{12}$$

where R_j is the armature winding resistance of the motor, and i_{qj} and i_{dj} are the q- and d-axis current of the motor, respectively. In (12), we assumed that the copper loss in the q-axis is much bigger than that in the d-axis.

Suppose that the magnet torque is much greater than the reluctance torque.[1] Then, the following relationship between the q-axis current and torque is obtained:

$$i_{qj} = \frac{T_j}{K_{tj}} = \frac{T_j}{p_{nj}\Psi_j} \tag{13}$$

where K_{tj} is the torque coefficient of the motor, p_{nj} is the number of pole pairs, and Ψ_j is the interlinkage magnetic flux. Therefore, the copper loss P_c is given by

$$P_c = 2\sum_{j=f,r}\frac{R_j T_j^2}{K_{tj}^2}. \tag{14}$$

In this paper, the equivalent circuit model [18] was used to examine the iron loss. Fig. 5 shows the d- and q-axis equivalent circuits of the permanent-magnet motor. From the circuits, the sum of iron loss P_i is expressed as

$$P_i = 2\sum_{j=f,r}\frac{\omega_{ej}^2}{R_{cj}}\left\{(L_{qj}i_{oqj})^2 + (L_{dj}i_{odj} + \Psi_j)^2\right\} \tag{15}$$

where ω_{ej} is the electrical angular velocity of the motor, R_{cj} is the equivalent iron loss resistance, L_{dj} is the d-axis inductance, and L_{qj} is the q-axis inductance [18]. i_{odj} and i_{oqj} are defined in Fig. 5. The first and second terms in (15) represent the q- and d-axis iron losses, respectively.

In (15), the armature reaction of the d-axis $\omega_e L_d i_{od}$ is neglected since it is much smaller than the electromotive force of the magnet $\omega_e\Psi$. In the modeling of the iron loss, ω_{ej} was approximated as $p_{nj}V/r$ for simplicity since the slip ratio of each wheel was small.

[1] If this assumption and the approximation in (12) are not used, the analytic solution such as (21) cannot be obtained. In the case that these assumptions are not satisfied, the numerical optimization is possible, which is described in the Appendix.

Under these conditions, P_i is approximated by

$$P_i \approx 2\frac{V^2}{r^2}\sum_{j=f,r}\frac{p_{nj}^2}{R_{cj}}\left\{\left(\frac{L_{qj}}{K_{tj}}\right)^2 T_j^2 + \Psi_j^2\right\}. \quad (16)$$

Note that to obtain (16), $T_j = K_{tj} i_{oqj}$ is used instead of (13) because the iron loss resistance R_{cj} is considered here. The equivalent iron loss resistance R_{cj} is expressed as

$$\frac{1}{R_{cj}(\omega_{ej})} = \frac{1}{R_{c0j}} + \frac{1}{R'_{c1j}|\omega_{ej}|}. \quad (17)$$

In (17), the first and second terms on the right-hand side represent the eddy current loss and hysteresis loss, respectively [19]. By applying $\omega_{ej} = p_{nj}V/r$, R_{cj} is expressed as $R_{cj}(V)$.

From the above equations, P_{in} is expressed as

$$\begin{aligned} P_{\text{in}} &= P_{\text{out}} + P_c + P_i \\ &= 2\sum_{j=f,r}\omega_j T_j + 2\sum_{j=f,r}\frac{R_j T_j^2}{K_{tj}^2} \\ &\quad + 2\frac{V^2}{r^2}\sum_{j=f,r}\frac{p_{nj}^2}{R_{cj}}\left\{\left(\frac{L_{qj}}{K_{tj}}\right)^2 T_j^2 + \Psi_j^2\right\}. \end{aligned} \quad (18)$$

III. Optimization of Front and Rear Driving–Braking Force Distributions

A. Derivation of Optimal Distribution Ratio

The optimal driving–braking force distribution ratio that minimizes the input power of the inverter is derived here. To derive the optimal distribution ratio, the inertia force of each wheel is neglected in (1) because $J_{\omega_j}\dot{\omega}_j \ll rF_j$ under a high-μ load. As noted in [20], the denominator of (4) can be approximated to V when $|\lambda_j| \ll 1$. Therefore, T_j and ω_j can be approximated as

$$T_j = rF_j \quad (19)$$

$$\omega_j = \frac{V}{r}(1+\lambda_j). \quad (20)$$

By applying the above approximation, P_{in} is obtained as $P_{\text{in}}(k)$ [16]. Since $P_{\text{in}}(k)$ is a quadratic function of k, the optimal distribution ratio k_{opt} satisfies $\partial P_{\text{in}}/\partial k|_{k=k_{\text{opt}}} = 0$. Therefore, k_{opt} is derived as a function of V and a_x [16], i.e.,

$$k_{\text{opt}}(V, a_x) = \frac{\frac{V}{D'_s N_f(a_x)} + \frac{r^2 R_f}{K_{tf}^2} + \frac{V^2}{R_{cf}(V)}\left(\frac{L_{qf}}{\Psi_f}\right)^2}{\frac{V}{D'_s}\sum_{j=f,r}\frac{1}{N_j(a_x)} + r^2\sum_{j=f,r}\frac{R_j}{K_{tj}^2} + V^2\sum_{j=f,r}\frac{1}{R_{cj}(V)}\left(\frac{L_{qj}}{\Psi_j}\right)^2}. \quad (21)$$

B. Numerical Calculation

Fig. 6 shows the calculation results of the experimental vehicle's motor efficiencies when R_{c0j} was 300 Ω and R'_{c1f} and R'_{c1r} were 0.13 and 0.053 Ωs/rad, respectively. In Figs. 1 and 6, the front motor had a higher global efficiency than the rear motor because the former can have a much smaller internal diameter than the latter. Therefore, the number of turns of the motor windings and the teeth shape can be optimized for the front-motor design. Fig. 7 shows the modeling error of the motor efficiency, which was calculated by subtracting the measured value from the calculated value. In Fig. 7, the calculation error was within ±5% for most evaluated operation areas. Therefore, the modeling in this study properly expressed the motor characteristics.

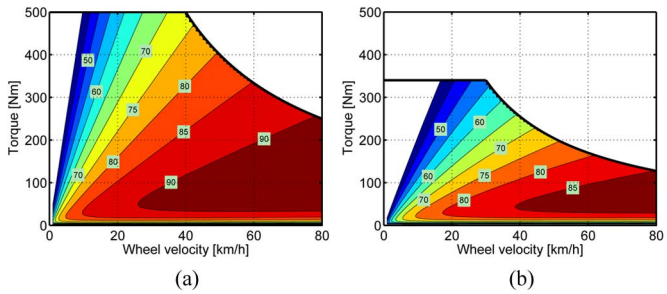

Fig. 6. Motor efficiency (calculated). (a) Front motor. (b) Rear motor.

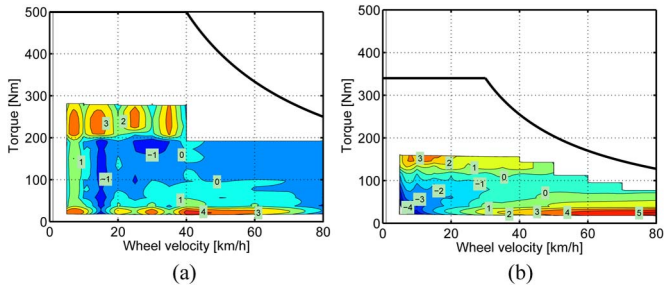

Fig. 7. Modeling error of motor efficiency. (a) Front motor. (b) Rear motor.

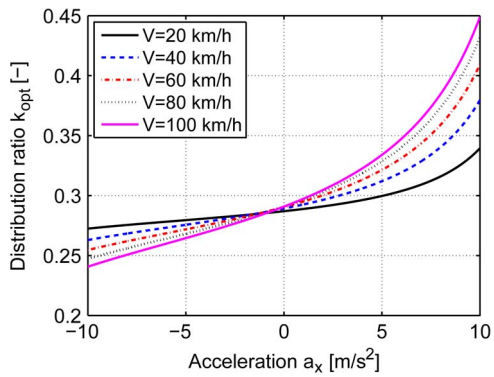

Fig. 8. Optimal distribution ratio k_{opt}.

Fig. 8 shows the calculated k_{opt}. Under a high-μ load, the normalized driving stiffness D'_s was set to 12. k_{opt} increased with acceleration and decreased with increased deceleration. This is mainly because of the influence of the variation in the slip ratio due to load transfer and copper loss. On the other hand, k_{opt} increased with vehicle velocity. The range of k_{opt} was 0.2–0.45. This is because the front motor had higher efficiency than the rear motor in a wide area of the efficiency map, as shown in Fig. 1.

IV. Experiment

A. Test Field and Test Bench

A test field for vehicles owned by the National Traffic Safety and Environment Laboratory in Japan was used for the field test, which is shown in Fig. 9(a). This test field has a

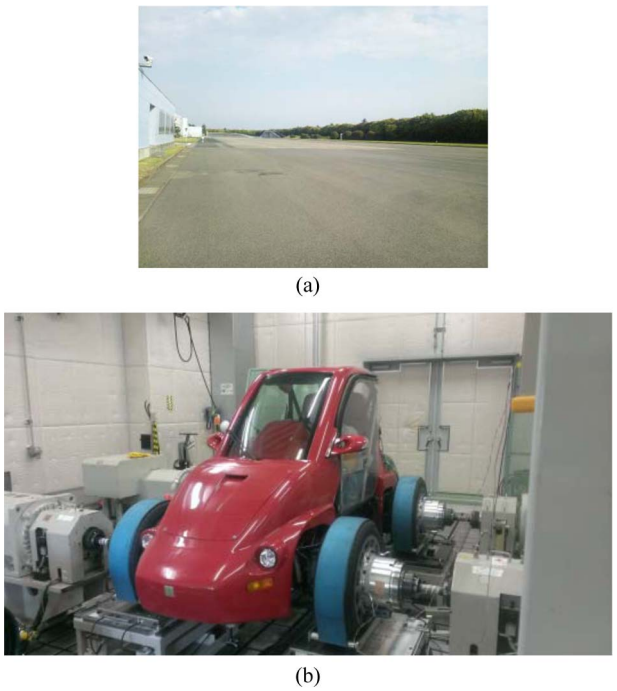

Fig. 9. Test field and bench test environment. (a) Test field. (b) Test vehicle and RC-S.

1350-m-long straight road, a low-μ load, and a slope. This field allows experiments to be performed under various driving conditions. In this paper, no-slope and high-μ road conditions were employed for the evaluation.

In the bench test, the Real Car Simulation Bench (RC-S) owned by Ono Sokki Co., Ltd. was used. Fig. 9(b) shows the bench test environment. In the experiments using RC-S, driving shafts were directly connected to dynamometers through a bearing wheel, which is different from the case of a chassis dynamometer. By changing the vehicle model of RC-S, experiments can be conducted under various road conditions. In addition, RC-S can control dynamos with a faster response than a chassis dynamometer using rollers, which have greater inertia. Therefore, RC-S is suitable for the bench test of EVs driven by motors. In this research, the test bench was very useful because the experiments were not influenced by changes in the wind and road conditions.

Fig. 10 shows the block diagram of the experimental environment using RC-S. The motor torque of each wheel was measured by a torque meter and input to the vehicle model of RC-S. The velocity and acceleration of the vehicle were calculated by vehicle dynamics model in RC-S. In order to control the motors, these values were input to the vehicle controller.

B. Driving Resistance

For the simulation and bench test, the driving resistance of the test vehicle was measured in the test field. The driving resistance F_{DR} can be determined by

$$F_{\mathrm{DR}}(V) = \mu_0 Mg + \frac{1}{2}\rho C_d A V^2 \tag{22}$$

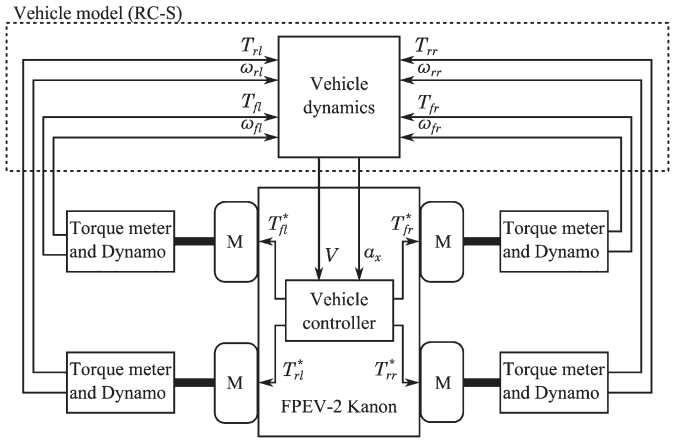

Fig. 10. Block diagram of experiment environment.

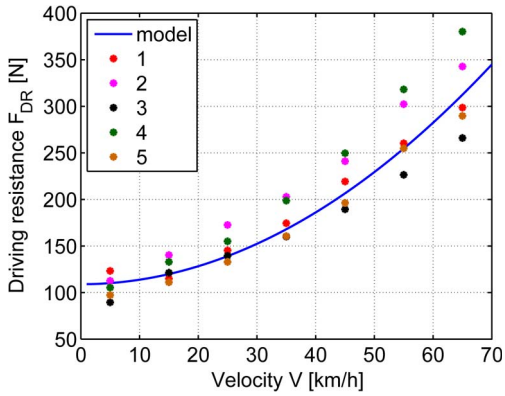

Fig. 11. Comparison of model and measurement results of driving resistance.

where μ_0 is the rolling-friction coefficient, ρ is the air density, C_d is the drag coefficient, and A is the frontal projected area. ρ and A were determined to be 1.205 kg/m^3 and 1.2 m^2, respectively. μ_0 and C_d were 1.28×10^{-2} and 0.863, respectively. These values were empirically obtained. Fig. 11 shows the measured and calculated driving resistance values. The measurements were taken five times. As shown in the figure, the model described by (22) matched the measured values.

C. Input Power for Change in Distribution Ratio

Fig. 12 shows the experimental results of P_{in} when the distribution ratio was changed. This experiment was conducted using RC-S. The inverter input power P_{in} can be calculated as

$$P_{\mathrm{in}} = V_{\mathrm{dc}} \sum_{j=f,r} I_{\mathrm{dc}j} \tag{23}$$

where V_{dc} is the inverter input voltage, and $I_{\mathrm{dc}j}$ is the front and rear inverter input currents. Fig. 12 shows the results when a_x and V were 1.5 m/s^2 and 40 km/h, respectively, and -2.0 m/s^2 and 40 km/h, respectively. These conditions were simulated by RC-S. In Fig. 12, the rigid lines represent the calculation results of the computer simulation; here, the approximations presented above were not applied. The value at k_{opt} calculated by (21) is shown as a dashed line. Fig. 12 indicates that P_{in} is a convex function of k. Therefore, a k value

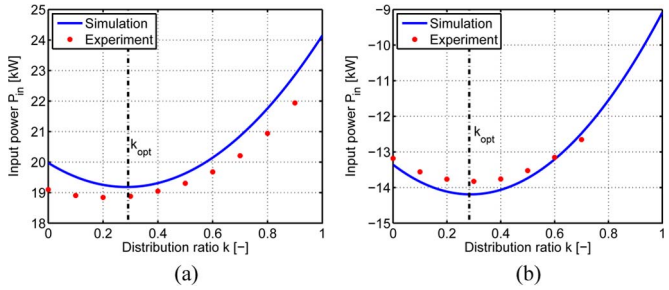

Fig. 12. Experimental result of $P_{\rm in}$. (a) $a_x = 1.5$ m/s^2, $V = 40$ km/h. (b) $a_x = -2.0$ m/s^2, $V = 40$ km/h.

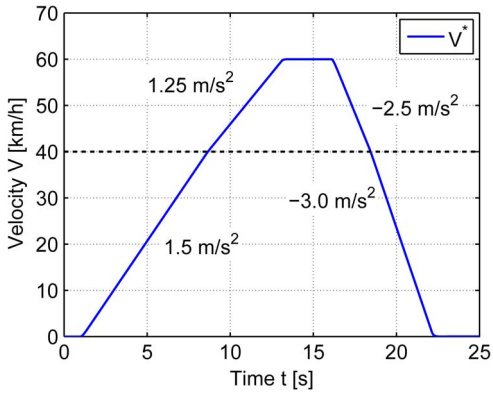

Fig. 13. Reference vehicle speed.

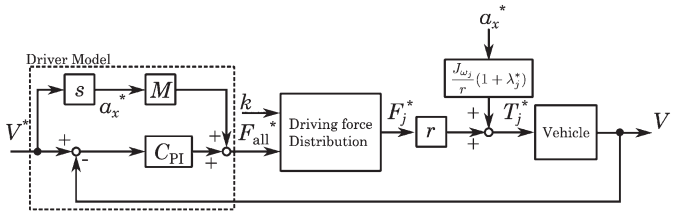

Fig. 14. Vehicle speed control system.

that minimizes $P_{\rm in}$ exists. In the simulation, although there were errors caused by the approximations of the torque, wheel angular velocity, copper loss, and iron loss, the case of $k = k_{\rm opt}$ showed almost equal minimum values, as shown in Fig. 12. The experimental results indicate that $k_{\rm opt}$ can mostly minimize the input power, although a little error remains present. Therefore, the approximations assumed in this study were appropriate.

D. Pattern Driving

To demonstrate the effectiveness of the proposed system, the driving cycle was evaluated with both the test field and test bench. Fig. 13 shows the driving cycle, which comprised two-step acceleration, cruising, and two-step deceleration. The accelerations were 1.5 and 1.25 m/s^2, the maximum vehicle speed was 60 km/h, and the decelerations were -2.5 and -3.0 m/s^2. The cases of $k = 0$, 0.1,0.2,0.3,0.4,0.5, and $k_{\rm opt}$ were evaluated. In the bench test, the driving resistance was set to the value measured in the field test.

Fig. 14 shows the vehicle velocity control system for determining the vehicle velocity pattern in Fig. 13 during the field test. This system comprised a feedforward controller and a feedback controller. These controllers corresponded to the driver model. The input was the vehicle velocity reference V^*, and the average of all of the wheel velocities was used as the vehicle velocity V in the field test. The value calculated with the vehicle model was used in the bench test. These controllers generated the total reference driving–braking force $F^*_{\rm all}$. Then, $F^*_{\rm all}$ was distributed to the reference front and rear driving–braking forces F^*_j based on (8) and (9). Represented by the slip ratio, the reference front and rear torques T^*_j are given by

$$T^*_j = rF^*_j + \frac{J_{\omega_j} a^*_x}{r}\left(1 + \lambda^*_j\right) \tag{24}$$

where the second term of the right-hand side represents the compensation for the inertia torque of the wheels [20]. In order to consider the stability of the vehicle velocity control system, the reference acceleration a^*_x and slip ratio λ^*_j were substituted for their measured values. Because $J_{\omega_j} a^*_x / r$ was much smaller than rF^*_j, the second term did not have a large effect. Therefore, λ^*_j was simply set to 0.05, 0, and -0.05 during acceleration, cruising, and deceleration, respectively.

The vehicle velocity controller $C_{\rm PI}(s)$ was a proportional-integral (PI) controller that was designed by the pole placement method. The plant of the vehicle velocity controller is given by

$$\frac{V}{F_{\rm all}} = \frac{1}{Ms}. \tag{25}$$

The pole of vehicle velocity controller was set to -5 rad/s.

Fig. 15 shows the vehicle speed control system for the experiments using RC-S. The inverters and motors of the real vehicle and vehicle model in RC-S represent the actual vehicle plant in Fig. 14. The vehicle model comprised the equations given in Section II.

Fig. 16 shows the experimental results for the vehicle motion in the field and bench tests; the results of each test when $k = k_{\rm opt}$ are shown. Fig. 16(a) shows the vehicle velocity. In each test, the vehicle velocity followed the reference, similar to the simulation results. This figure also shows the distribution ratio. The optimal distribution ratio $k_{\rm opt}$ increased during acceleration and decreased during deceleration. This result matched the previous calculations. Fig. 16(c) and (d) shows the front and rear driving–braking forces, respectively. The total driving–braking force $F_{\rm all}$ was distributed based on k. In addition, the absolute values of the driving force in the simulation and bench test were equal to that of the field test. Therefore, the driving resistance model was appropriate, and the test bench realized the same load as the field test.

Fig. 17 shows the energy consumption in each experimental test. The energy consumptions during acceleration, cruising, and deceleration are shown separately. In order to confirm the reproducibility of the experimental results, the average values and standard deviations, shown as error bars, were calculated for the field and bench tests, which were carried out 12 and 8 times, respectively. In the computer simulation and RC-S, the energy consumption and regenerated energy during each driving section were minimized and maximized by the proposed system. In the field test, the effectiveness of the proposed system with regard to the total energy consumption was not

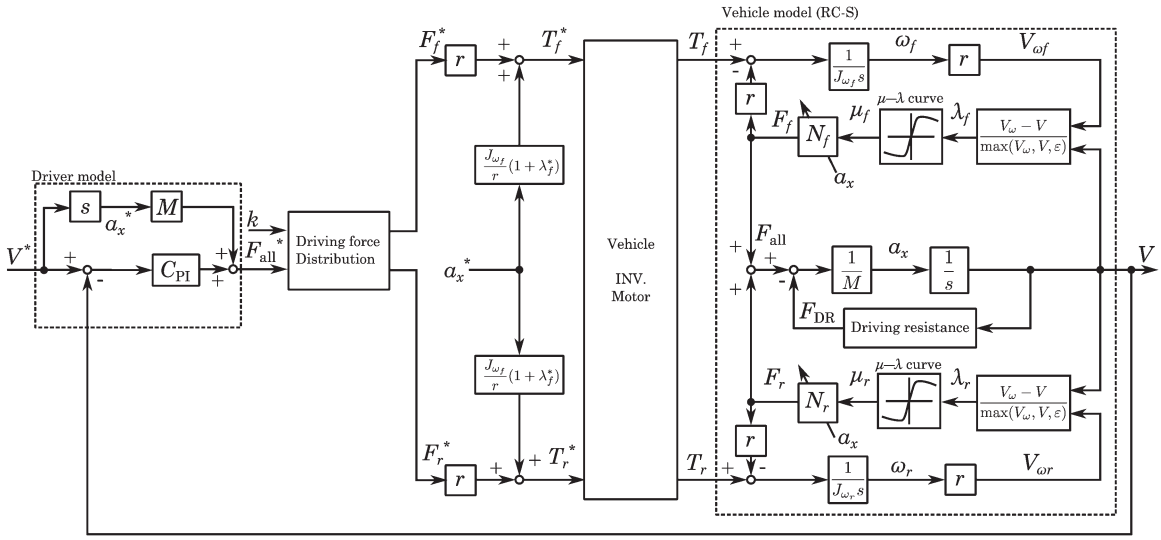

Fig. 15. Vehicle speed control system and vehicle model of RC-S.

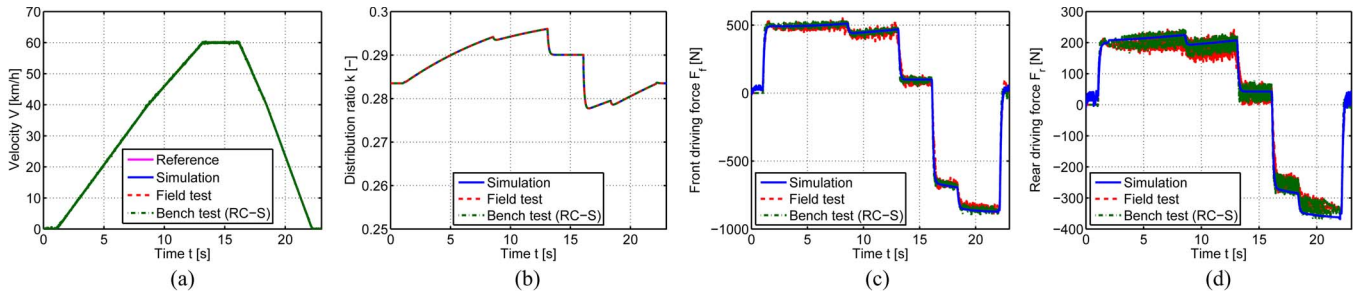

Fig. 16. Experimental results related to vehicle motion of driving pattern $(k = k_{\mathrm{opt}})$. (a) Velocity. (b) Distribution ratio. (c) Front driving force. (d) Rear driving force.

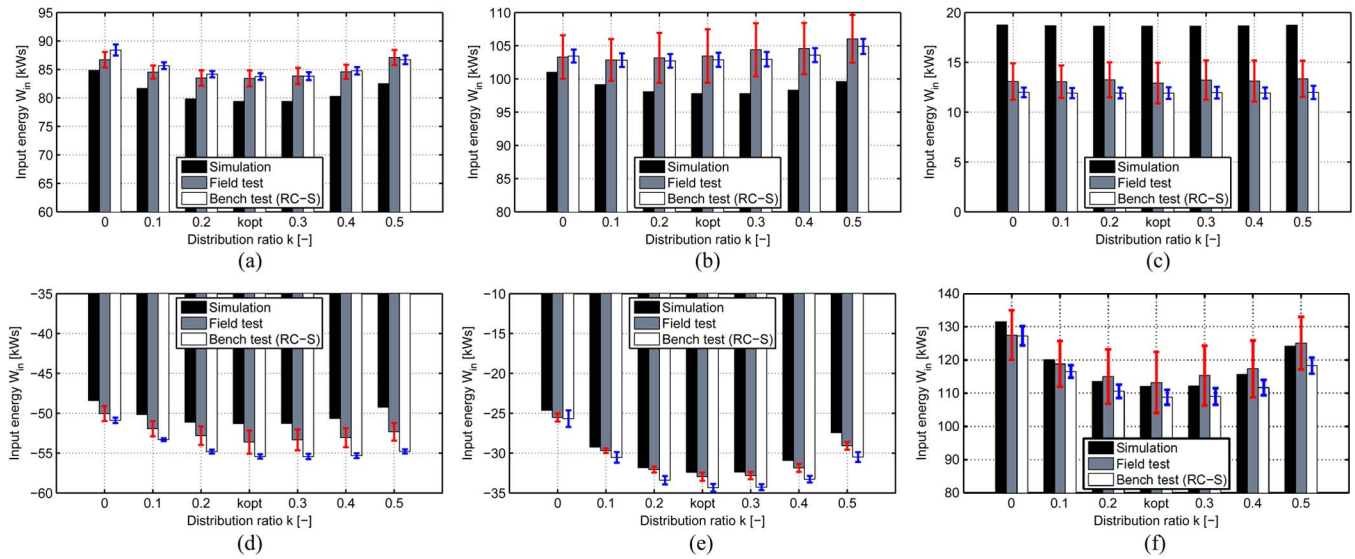

Fig. 17. Experimental results of pattern driving (comparison of energy consumption). (a) Acceleration 1 (1.5 m/s^2, 0–40 km/h). (b) Acceleration 2 (1.25 m/s^2, 40–60 km/h). (c) Cruising (60 km/h, 3 s). (d) Deceleration 1 (-2.5 m/s^2, 60–40 km/h). (e) Deceleration 2 (-3.0 m/s^2, 40–0 km/h). (f) Total.

clear because of the large dispersion for the data. However, Fig. 17(a) and (e) clearly shows the effectiveness in the case of large acceleration because the variations in the wind and road conditions on the energy consumption was relatively small with a large torque. In the computer simulation results, the high-speed operation showed worse efficiency than the experimental results. This is because the simulation model had greater iron loss than the actual values. A comparison of the simulation and two tests showed that their energy consumptions roughly agreed. Thus, the proposed system achieved 9% and 8% decreases in the energy consumption during the bench and field tests, respectively, compared with $k = 0.5$.

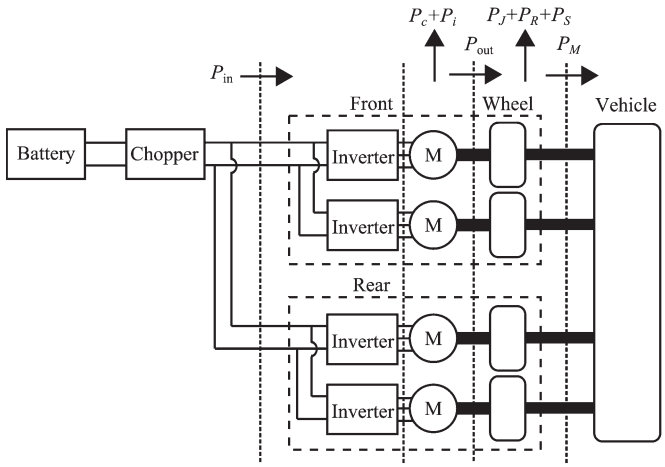

Fig. 18. Loss separation model.

E. Loss Separation

To analyze the effectiveness of the proposed system, loss separation was conducted. Fig. 18 shows the loss separation model. P_{out} can be separated as

$$P_{\text{out}} = P_M + P_J + P_R + P_S \tag{26}$$

where P_M is the power stored as kinetic energy of the vehicle mass, P_J is the sum of power stored as rotational energy of each wheel, P_R is the loss caused by the driving resistance, and P_S is the sum of the loss caused by the slip of each wheel.

Fig. 19 shows the calculated loss separation for the driving pattern simulation with $k = k_{\text{opt}}$. The input energy W_x (x was replaced by c, i, out, M, J, R, or S) was calculated by

$$W_x = \int_{t_s}^{t_e} P_x dt \tag{27}$$

where t_s and t_e are the start and end times, respectively, of integration. In Fig. 19, W_{out} and W_M accounted for most of W_{in} and W_{out}, respectively. In the results for acceleration 1 and deceleration 2, the ratio of W_c was comparatively large because of the larger acceleration or deceleration. On the other hand, W_R accounted for most of W_{in} during cruising. W_J and W_S were small relative to the other losses in all sections. Although W_i was smaller than W_c in Fig. 19, W_i should be greater than W_c at higher speeds. In Fig. 19(f), the total of W_M and W_J was zero. The ratios of W_R, W_c, and W_i to W_{in} were about 40%, 40%, and 20%, respectively. W_S was very small. The above results clearly show that the driving resistance and copper loss accounted for most of the total loss.

F. Evaluation Based on JC08 Mode

The JC08 mode test, which is a major Japanese driving cycle, was employed for evaluation under more practical conditions. The average and maximum velocities of JC08 mode were 24.4 and 81.6 km/h, respectively. The driving distance was 8.172 km.

Table III shows the JC08 mode results. The test was conducted once for each of the two conditions $k = 0.5$ and k_{opt}. With the proposed system, the cruising range for 1 and 5.6 kWh (battery capacity of experimental vehicle) were extended by 0.4 and 2.3 km, respectively. These experimental results were almost equal to the simulation results. During real driving, the frequency of large accelerations or decelerations is higher than that of JC08 mode. Therefore, further improvement is expected under actual driving conditions.

V. Conclusion

This paper has proposed a model-based RECS for EVs that optimizes the front and rear driving–braking force distributions. The slip ratio of the wheels and the copper and iron losses of the motors are considered to minimize the energy consumption. Because the proposed distribution method only depends on vehicle acceleration and velocity, the distribution ratios during the acceleration or deceleration processes can be optimized.

A bench test was carried out to realize results with high reproducibility. The results of a computer simulation, actual field test, and bench test were compared. The simulation and experimental results confirmed the effectiveness of the proposed system. The simulation and bench test results on the energy consumption matched the field test results.

Therefore, this study verified that the proposed system can extend the cruising range of EVs and accurately measure the energy consumption.

This paper only dealt with the case of front and rear distribution. The future work is to extend this method to the case of four-wheel distribution by combining our previous approach of left and right distribution [14].

Appendix
Generalization to the Case of $i_{dj} \neq 0$

When the reluctance torque is not negligible, motor torque T_j and motor loss P_{lossj} can be expressed as

$$T_j = K_{mtj} i_{oqj} + K_{rtj} i_{odj} i_{oqj} \tag{28}$$

$$P_{lossj} = P_{cj} + P_{ij} \tag{29}$$

$$P_{cj} = R_j \left(i_{dj}^2 + i_{qj}^2\right) \tag{30}$$

$$P_{ij} = \frac{\omega_{ej}^2}{R_{cj}} \left\{(L_{qj} i_{oqj})^2 + (L_{dj} i_{odj} + \Psi_j)^2\right\} \tag{31}$$

where $K_{mtj} := p_{nj}\Psi_j$, $K_{rtj} := p_{nj}(L_{dj} - L_{qj})$, and $\omega_{ej} = p_{nj}\omega_j$. On the equivalent circuit Fig. 5, when the required torque T_j is given, the driving condition of i_{odj} to minimize P_{lossj} is as follows [18]:

$$T_j^2 = \frac{AB}{C}$$

$$A := R_j R_{cj}^2 i_{odj} + \omega_{ej}^2 L_{dj}(R_j + R_{cj})(L_{dj} i_{odj} + \Psi_j)$$

$$B := p_{nj}^2 \left\{\Psi_j + (L_{dj} - L_{qj}) i_{odj}\right\}^3$$

$$C := \left\{\omega_{ej}^2 L_{qj}^2 (R_{cj} + R_j) + R_j R_{cj}^2\right\} (L_{dj} - L_{qj}). \tag{32}$$

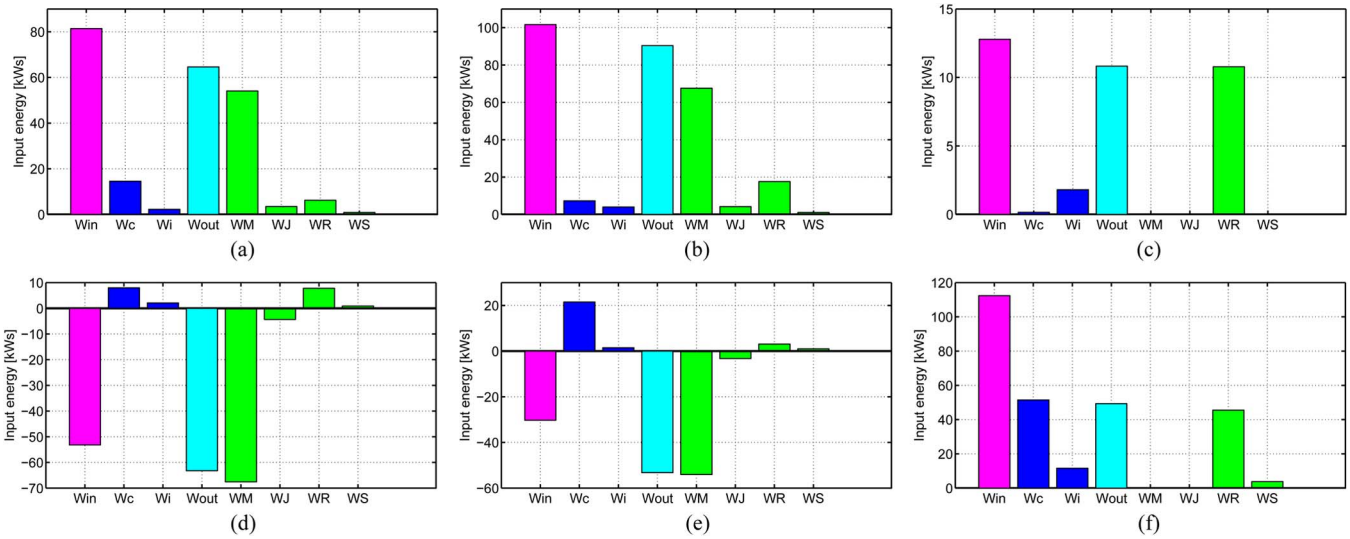

Fig. 19. Calculation results of loss separation during driving pattern simulation ($k = \mathrm{k}_{opt}$). (a) Acceleration 1 (1.5 m/s^2, 0–40 km/h). (b) Acceleration 2 (1.25 m/s^2, 40–60 km/h). (c) Cruising (60 km/h, 3 s). (d) Deceleration 1 (-2.5 m/s^2, 60–40 km/h). (e) Deceleration 2 (-3.0 m/s^2, 40–0 km/h). (f) Total.

TABLE III
CRUISING RANGE (JC08 MODE)

	Simulation		Bench test (RC-S)	
k	0.5	k_{opt}	0.5	k_{opt}
1 kWh	11.2 km	11.6 km	12.2 km	12.6 km
5.6 kWh	62.7 km	65.0 km	68.3 km	70.6 km

From (4), the wheel speed can be represented by

$$\omega_j = \frac{V}{r}\frac{1}{1-\lambda_j}. \tag{33}$$

Here, the definition of $r\omega_j > V$ in (4) is utilized. The wheel angular speed $\dot{\omega}_{oj}$ is obtained by

$$\dot{\omega}_j = \frac{a_x}{r}\frac{1}{1-\lambda_j} \tag{34}$$

where the approximation of $\dot{\lambda}_j \simeq 0$ is used because the road condition is assumed to be constant.

From (5) to (9), the slip ratios λ_f and λ_r are represented as

$$\lambda_f(k) = \frac{(1-k)lF_{\mathrm{all}}}{D'_{sf}M(l_r g - h_g a_x)} \tag{35}$$

$$\lambda_r(k) = \frac{klF_{\mathrm{all}}}{D'_{sr}M(l_f g + h_g a_x)}. \tag{36}$$

By substituting (35) and (36) for (33) and (34), we obtain

$$\omega_f(k) = \frac{V}{r}\frac{D'_{sf}M(l_r g - h_g a_x)}{D'_{sf}M(l_r g - h_g a_x) - (1-k)lF_{\mathrm{all}}} \tag{37}$$

$$\omega_r(k) = \frac{V}{r}\frac{D'_{sr}M(l_f g + h_g a_x)}{D'_{sr}M(l_f g + h_g a_x) - klF_{\mathrm{all}}} \tag{38}$$

$$\dot{\omega}_f(k) = \frac{a_x}{r}\frac{D'_{sf}M(l_r g - h_g a_x)}{D'_{sf}M(l_r g - h_g a_x) - (1-k)lF_{\mathrm{all}}} \tag{39}$$

$$\dot{\omega}_r(k) = \frac{a_x}{r}\frac{D'_{sr}M(l_f g + h_g a_x)}{D'_{sr}M(l_f g + h_g a_x) - klF_{\mathrm{all}}}. \tag{40}$$

From the above equations and (1), the front and rear torques are represented as the function of k by

$$T_f(k) = \frac{J_{\omega_f} a_x D'_{sf} M(l_r g - h_g a_x)}{r\left\{D'_{sf}M(l_r g - h_g a_x) - (1-k)lF_{\mathrm{all}}\right\}} + \frac{(1-k)rF_{\mathrm{all}}}{2} \tag{41}$$

$$T_r(k) = \frac{J_{\omega_r} a_x D'_{sr} M(l_f g + h_g a_x)}{r\{D'_{sr}M(l_f g + h_g a_x) - klF_{\mathrm{all}}\}} + \frac{krF_{\mathrm{all}}}{2}. \tag{42}$$

Therefore, the motor outputs can also be functions of k as

$$P_{outf}(k) = \omega_f(k)T_f(k) \tag{43}$$

$$P_{outr}(k) = \omega_r(k)T_r(k). \tag{44}$$

Next, the motor losses are considered. From (28), the q-axis currents can be modeled by

$$i_{oqf}(k,\ i_{odf}) = \frac{T_f(k)}{K_{mt} + K_{rt} i_{odf}} \tag{45}$$

$$i_{oqr}(k,\ i_{odr}) = \frac{T_r(k)}{K_{mt} + K_{rt} i_{odr}}. \tag{46}$$

From (29) to (31), the motor losses P_{lossf} and P_{lossr} are represented by

$$P_{lossf}(k,\ i_{odf}) = P_{cf}(k,\ i_{odf}) + P_{if}(k,\ i_{odf}) \tag{47}$$

$$P_{lossr}(k,\ i_{odr}) = P_{cr}(k,\ i_{odr}) + P_{ir}(k,\ i_{odr}). \tag{48}$$

Note that each motor loss can be determined by k and d-axis current. Therefore, total input power can be modeled as

$$P_{in}(k,\ i_{odf},\ i_{odr}) = 2P_{outf}(k) + 2P_{outr}(k) + 2P_{lossf}(k,\ i_{odf}) + 2P_{lossr}(k,\ i_{odr}). \tag{49}$$

The optimal condition to minimize $P_{in}(k,\ i_{odf},\ i_{odr})$ is

$$\text{grad}\ P_{in}\left(k,\ i_{odf},\ i_{odr}\right) = \mathbf{0} \tag{50}$$

$$\frac{\partial P_{in}\left(k,\ i_{odf},\ i_{odr}\right)}{\partial k} = 0 \tag{51}$$

$$\frac{\partial P_{in}\left(k,\ i_{odf},\ i_{odr}\right)}{\partial i_{odf}} = \frac{\partial P_{lossf}(k,\ i_{odf})}{\partial i_{odf}} = 0 \tag{52}$$

$$\frac{\partial P_{in}\left(k,\ i_{odf},\ i_{odr}\right)}{\partial i_{odr}} = \frac{\partial P_{lossr}(k,\ i_{odr})}{\partial i_{odr}} = 0. \tag{53}$$

Equations (52) and (53) correspond with the minimum loss solution of each motor (32), which can be numerically solved as the function of k (i.e., $i_{odf}(k)$ and $i_{odr}(k)$). Therefore, the optimal k can also be numerically solved from (51). Because (51) becomes only the function of k, the online calculation cost can be reduced.

Acknowledgment

The authors would like to thank Dr. Y. Goto and D. Kawano of the National Traffic Safety and Environment Laboratory for the help with experiments in the test field; K. Sato and Y. Matsuo of Ono Sokki Company, Ltd. for the help with the bench tests; and Dr. T. Miyajima of our laboratory for the helpful discussion on the Appendix.

References

[1] Y. Hori, "Future vehicle driven by electricity and control—Research on four-wheel-motored, "UOT Electric March II"," *IEEE Trans. Ind. Electron.*, vol. 51, no. 5, pp. 954–962, Oct. 2004.

[2] K. Maeda, H. Fujimoto, and Y. Hori, "Four-wheel driving-force distribution method based on driving stiffness and slip ratio estimation for electric vehicle with in-wheel motors," in *Proc. IEEE VPPC*, Seoul, Korea, 2012, pp. 1286–1291.

[3] T. Hsiao, "Robust estimation and control of tire traction forces," *IEEE Trans. Veh. Technol.*, vol. 62, no. 3, pp. 1378–1383, Mar. 2013.

[4] J. Kang, J. Yoo, and K. Yi, "Driving control algorithm for maneuverability, lateral stability, rollover prevention of 4WD electric vehicles with independently driven front and rear wheels," *IEEE Trans. Veh. Technol.*, vol. 60, no. 7, pp. 2987–3001, Sep. 2011.

[5] K. Nam, H. Fujimoto, and Y. Hori, "Advanced motion control of electric vehicles based on robust lateral tire force control via active front steering," *IEEE/ASME Trans. Mechatronic*, vol. 19, no. 1, pp. 289–299, Feb. 2014.

[6] S. Chopa and P. Bauer, "Driving range extension of EV with on-road contactless power transfer—A case study," *IEEE Trans. Ind. Electron.*, vol. 60, no. 1, pp. 329–338, Jan. 2013.

[7] J. Shin *et al.*, "Design and implementation of shaped magnetic-resonance-based wireless power transfer system for roadway-powered moving electric vehicles," *IEEE Trans. Ind. Electron.*, vol. 61, no. 3, pp. 1179–1192, Mar. 2014.

[8] P. J. Grbovic, P. Delarue, P. L. Moigne, and P. Bartholomeus, "The ultracapacitor-based regenerative controlled electric drives with power-smoothing capability," *IEEE Trans. Ind. Electron.*, vol. 59, no. 12, pp. 4511–4522, Dec. 2012.

[9] J. Cao and A. Emadi, "A new battery/ultracapacitor hybrid energy storage system for electric, hybrid, plug-in hybrid electric vehicles," *IEEE Trans. Power Electron.*, vol. 27, no. 1, pp. 122–132, Jan. 2012.

[10] M. Montazeri, M. Soleymani, and S. Hashemi, "Impact of traffic conditions on the active suspension energy regeneration in hybrid electric vehicles," *IEEE Trans. Ind. Electron.*, vol. 60, no. 10, pp. 4546–4553, 2013.

[11] H. Toda, Y. Oda, M. Kohno, M. Ishida, and Y. Zaizen, "A new high flux density non-oriented electrical steel sheet and its motor performance," *IEEE Trans. Magn.*, vol. 48, no. 11, pp. 3060–3063, Nov. 2012.

[12] K. Inoue, K. Kotera, Y. Asano, and T. Kato, "Optimal torque and rotating speed trajectories minimizing energy loss of induction motor under both torque and speed limits," in *Proc IEEE PEDS*, 2013, pp. 1127–1132.

[13] X. Yuan and J. Wang, "Torque distribution strategy for a front- and rear-wheel-driven electric vehicle," *IEEE Trans. Veh. Technol.*, vol. 61, no. 8, pp. 3365–3374, Oct. 2012.

[14] H. Fujimoto and H. Sumiya, "Range extension control system of electric vehicle based on optimal torque distribution and cornering resistance minimization," in *Proc. IEEE IECON*, 2011, pp. 3727–3732.

[15] H. Fujimoto, S. Egami, J. Saito, and K. Handa, "Range extension control system for electric vehicle based on searching algorithm of optimal front and rear driving force distribution," in *Proc. IEEE IECON*, 2012, pp. 4244–4249.

[16] S. Harada and H. Fujimoto, "Range extension control system for electric vehicle on acceleration and deceleration based on front and rear driving/braking force distribution considering slip ratio and motor loss," in *Proc. IEEE IECON*, 2013, pp. 6624–6629.

[17] H. B. Pacejka and E. Bakker, "The magic formula tyre model," *Veh. Syst. Dyn.*, vol. 21, no. 1, pp. 1–18, 1992.

[18] S. Morimoto, Y. Tong, Y. Takeda, and T. Hirasa, "Loss minimization control of permanent magnet synchronous motor drives," *IEEE Trans. Ind. Electron.*, vol. 41, no. 5, pp. 511–517, Oct. 1994.

[19] C. Kaido, "Effects of cores on the characteristics of an induction VCM," *IEEE Transl. J. Magn. Jpn.*, vol. 9, no. 6, pp. 110–116, Nov./Dec. 1994.

[20] H. Fujimoto, J. Amada, and K. Maeda, "Review of traction and braking control for electric vehicle," in *Proc. IEEE VPPC*, Seoul, Korea, 2012, pp. 1292–1299.

Hiroshi Fujimoto (S'99–M'01–SM'12) received the Ph.D. degree from the Department of Electrical Engineering, The University of Tokyo, Chiba, Japan, in 2001.

In 2001, he joined the Department of Electrical Engineering, Nagaoka University of Technology, Niigata, Japan, as a Research Associate. From 2002 to 2003, he was a Visiting Scholar with the School of Mechanical Engineering, Purdue University, West Lafayette, IN, USA. In 2004, he joined the Department of Electrical and Computer Engineering, Yokohama National University, Yokohama, Japan, as a Lecturer and went on to become an Associate Professor in 2005. Since 2010, he has been an Associate Professor with The University of Tokyo, Chiba. His interests include control engineering, motion control, nanoscale servo systems, electric vehicle control, and motor drives.

Dr. Fujimoto received the Best Paper Award from the IEEE TRANSACTIONS ON INDUSTRIAL ELECTRONICS in 2001 and 2013, the Isao Takahashi Power Electronics Award in 2010, and the Best Author Prize of the Society of Instrument and Control Engineers (SICE) in 2010. He is a member of the SICE, the Robotics Society of Japan, and the Society of Automotive Engineers of Japan and a Senior Member of the Institute of Electrical Engineers of Japan.

Shingo Harada (S'13) received the B.S. degree in engineering from Gunma National College of Technology, Japan, in 2012 and the M.S. degree from The University of Tokyo, Chiba, Japan, in 2014.

He is currently with Mitsubishi Electric Corporation, Himeji, Japan.